Laser Generation of Sub-Micrometer Wrinkles in a Chalcogenide Glass Film as Physical Unclonable Functions

Paloma Martinez, Irene D Papagiannouli, Dominique Descamps, Stephane Petit, Joel Marthelot, Anna Lévy, Baptiste Fabre, Jean-Baptiste Dory, Nicolas Bernier, Jean-yves Raty, et al.

Laser generation of sub-micron wrinkles in a chalcogenide glass film as physical unclonable functions

*Paloma Martinez, Irene Papagiannouli, Dominique Descamps, Stéphane Petit, Joël Marthelot, Anna Lévy, Baptiste Fabre, Jean-Baptiste Dory, Nicolas Bernier, Jean-Yves Raty, Pierre Noé and Jérôme Gaudin**

P. Martinez , Dr. I. Papagiannouli, Dr. D. Descamps, Dr. S. Petit, Dr. B. Fabre, Dr. J. Gaudin
CELIA, Université Bordeaux, CEA, CNRS, UMR 5107, 351 Cours de la Libération, F-33405 Talence, France
E-mail: jerome.gaudin@u-bordeaux.fr

Dr. J. Marthelot
Aix-Marseille Univ., CNRS, IUSTI, F-13013 Marseille, France

Dr. A. Lévy
Sorbonne Université, CNRS, Institut des NanoSciences de Paris, INSP, Campus Pierre et Marie Curie, F-75252 Paris Cedex 05, FRANCE

Dr J.-B. Dory, Dr. N. Bernier, Dr. J.-Y. Raty, Dr. P. Noé
Université Grenoble Alpes, CEA-LETI, 17 rue des Martyrs, F-38054 Grenoble Cedex 9, France
E-mail: pierre.noe@cea.fr

Dr. J.-Y. Raty
Physics of Solids Interfaces and Nanostructures
CESAM group University of Liege
Allée du 6 Août 19, 4000 Sart-Tilman, Belgium

Keywords: physical unclonable functions, chalcogenide materials, silicon nitride, laser matter interaction, neural network

Laser interaction with solids is nowadays routinely used for functionalizing surfaces of materials.[1] In most cases, the generation of patterns/structures is the key feature to endow materials with specific features like hardening, super hydrophobicity, plasmonic colour enhancement or dedicated functions like anti-counterfeiting tags. We present a way to generate random patterns, resulting from the formation of wrinkles on the surface induced by laser melting of amorphous Ge-based chalcogenide thin films. These patterns, similar to fingerprints, are modulations of the surface height by tens of nm with a sub-µm periodicity.

We show that the spatial frequency of the patterns depends on the thickness of the melted layer, which can be tuned by varying the impinging laser fluence. The randomness of these patterns makes them an excellent candidate for the generation of physical unclonable function tags (PUF-tags) for anti-counterfeiting applications. We tested two specific ways to identify the PUF-tag: one with a cross-correlation procedure, another one using a neural network. In both cases, we demonstrate that the PUF-tag can be compared to a reference image (PUF-key) and identified with a high recognition ratio on most real application conditions. This paves the way to straightforward non-deterministic PUF-tag generation dedicated to small sensitive parts such as for example electronic devices/components, jewellery or watchmaking.

Patterning of surfaces is one of the most straightforward ways to functionalize material properties for aesthetic or practical purposes. Modern surface patterning methods involve etching, film deposition and lithography that is a non-exhaustive list. Each method can be achieved by various techniques as in the case of etching one can use laser,[1] ion[2] or electron[3] beams. Each technique has its own advantages and drawbacks that are beyond the scope of this contribution to present explicitly. One of the specific applications of surface patterning is the generation of truly random structures. True randomness is not a straightforward achievable property. The concept of physical unclonable function (PUF), also known as physical one-way function (POWF),[4] coined in this context the idea of using a non-stochastic physical[5] (or chemical[4]) process to generate a secured tag. Since then, numerous practical implementations of this concept thrived ranging from using the pristine surface state or randomly distributed nanostructures to wrinkles from polymer films[6] to mention only about surface related ideas. Wrinkles have been shown to form biomimetic micro-fingerprints especially well-suited for anti-counterfeiting. They present the advantage of a

straightforward reading procedure as a simple optical microscope is required to read and identify the PUF-tag. The method to create these wrinkles relies on the mechanical instabilities arising from the stress resistances of a bilayer structure made of a thin layer metal deposited on a elastomeric polymer,[7] or also from a laser-melted layer capped by a rigid oxide layer.[8–10] Numerous studies have been dedicated to wrinkles motivated by the understanding of the underlying physical process,[7,11] development of new methods[12] or possible applications.[4]

Here, we demonstrate a straightforward way to generate PUF-tags via formation of wrinkles on chalcogenide materials, i.e semiconductor alloys containing at least one chalcogen chemical element from group VI (S, Se and Te) alloyed for example with group IV or V elements like Ge, As or Sb atoms. These alloys have been routinely used in data storage like rewritable DVDs. More recently, they are at the origin of innovative phase-change memory devices[13,14] that enabled a real breakthrough in the memory technology field,[15] as well as opening new opportunities for photonic applications.[16,17]Wrinkles in these materials have already been observed,[18,19] but not really investigated while deterministic sub-micron laser patterning has been achieved.[20,21]

We observe the formation of wrinkles for two laser wavelengths and different pulse durations from 30 fs to 400 ps and for different types of chalcogenide alloys. We show that an irradiation by a single laser pulse can generate sub-µm period patterns. Finally, we test the uniqueness of the generated pattern in view of PUF-tag application. An open-source standard Fourier Mellin transform recognition algorithm shows to be sufficient to identify and certify the uniqueness of each pattern on a 200-tag sample. In order to gain speed and versatility, a deep learning strategy based on convolutional neural networks was developed and trained on the same experimental set of PUF and was shown to give excellent

performances.

The working principle of the experimental setup used to induce the patterns is schematized in **Figure 1-A**. The 1 kHz laser beam is focused on the sample surface rotating in order to irradiate a given area with a single laser pulse. Three different pulse energies were used: 18, 21 and 26 µJ resulting in fluences of F_0 = 21, 25 and 30 mJ.cm^{-2}. We note that experiments were also performed at 17 mJ.cm^{-2}, which did not result in the formation of patterns. As a result, the fluences in the range 17 mJ.cm^{-2} < F_{th} < 20 mJ.cm^{-2} are close to F_{th} the fluence melting threshold. The laser pulse duration was varied in the range of 30 fs to 400 ps. To avoid any possible effect of the Si (100) substrate, the amorphous GeTe layer was 500 nm thick, deposited by magnetron sputtering. The patterns shown in Figure 1-B result from the interaction of a 25 fs, 800 nm laser pulse with an as-deposited amorphous GeTe thin film sample. Other examples for chalcogenide alloys and various laser parameters (in terms of wavelength and pulse duration) are given in **Supporting Information (Figure S1)**, showing the universality of these patterns for such kinds of materials. We emphasize that similar experiments were also performed with an uncapped GeTe thin film sample, i.e. with no SiN capping layer, which resulted in no formation of wrinkles.

In **Figure 1-B**, the optical microscopy images of the irradiated area of the sample clearly show a change of colour compared to the pristine material and larger than the wrinkled area. This colour difference results from the modification of the optical refractive index of the material that is indicative of a local structural change due to laser irradiation. Therefore, the irradiated area was analysed by means of high-angle annular dark-field scanning transmission electron microscopy (STEM-HAADF). For that purpose, a foil of the centre of a pattern obtained at 30 mJ.cm^{-2} was prepared by means of focused ion beam technique (FIB). The STEM-HAADF image is shown in **Figure 1-C.** This image reveals no significant change of

the structure after irradiation, i.e. the thin film is still amorphous. This is further evidenced by the local electron diffraction pattern (**Figure 1-D**) acquired in points 1 and 2 (as shown on the STEM-HAADF image of **Figure 1-C)**: only diffuse scattering rings are visible on the electron diffraction patterns with no evidence of diffraction pattern coming from the crystalline phase that could have resulted from local material recrystallization. The sample is still amorphous in the irradiated area but, based on the optical contrast observed by the optical microscopy measurements, one can conclude that this is not the same amorphous structure. Furthermore, electron energy loss spectroscopy (EELS) maps (see the **Supporting Information Figure S2**) do not show any modification in composition in the irradiated area compared with the pristine layer evidencing that no chemical element segregation occurred due to laser irradiation. For Ge-Sb-Te chalcogenide phase-change materials lying on the GeTe-Sb_2Te_3 pseudo-binary line from which belong the GeTe and $Ge_2Sb_2Te_5$ (GST) compounds studied here it has been shown that the amorphous structure of the "as deposited" material obtained by magnetron sputtering differs from that of the "melt-quenched" state.[22] We can safely infer here that melting occurred after the laser irradiation leading to phase transition between the two amorphous phases, namely, as-deposited and melt-quenched phases. Another important observation from the STEM images is that the SiN capping layer is still present and intact. It results from the low absorbance of SiN at 800 nm wavelength.

In addition, in order to study the surface of the irradiated area, we used atomic force microscopy (AFM) to measure the surface relief. **Figure 1-E** shows a 20 × 20 μm^2 AFM image acquired in an area corresponding to the dashed square reported on the optical microscopy image (**Figure 1-B**) as well as a 5 × 5 μm^2 AFM image acquired at the very centre of the pattern. The vertical amplitude of the wrinkles is up to 70 nm in the centre of the pattern

and progressively decreases down to a few nanometers when going from the centre toward the pattern's edge.

Another interesting feature is that the wrinkles' spatial frequency also changes with the radius. In order to quantify this dependence we applied to the optical microscopy image a circular mask in order to select a specific area at a given radius (**Figure 2-A**). Each selected radial area corresponds to a constant fluence, which can be calculated since the laser beam profile is Gaussian (**Figure 2-B**). Then, a 2D-Fast Fourier Transform (2D-FFT) is applied to the filtered image (**Figure 2-C**). As shown in **Figure 2-C**, the radial integration of the 2D-FFT power spectrum clearly shows a peak at a given spatial frequency with a certain dispersion. Repeating the analysis for different masks (different radial values), the **Figure 2-D** shows the spatial frequency peak versus fluence for the three nominal fluences F_0 = 21, 25 and 30 mJ.cm^{-2}. The three as obtained curves plotted in the **Figure 2-D** are nearly overlapping, apart a slight shift visible at the low fluence values for the 30 mJ.cm^{-2} case. Above 20 mJ.cm^{-2} the two other curves obtained for irradiated samples at F_0 = 21 and 25 mJ.cm^{-2} are very similar. This slight discrepancy evidenced for the 30 mJ.cm^{-2} curve can be the result of a slight error in the beam center position which determines the value of the radius. Anyway, the fact that the three curves are similar clearly indicates that the fluence is the key parameter controlling the spatial frequency of the wrinkle patterns. As previously stated the wrinkles result from the surface melting of the GeTe film occurring as soon as the fluence is above or equal to F_{th}. The beam diameter is about a few tens of µm and the absorption depth determined from the extinction coefficient deduced from spectroscopic ellipsometry measurement (see **Figure S3** of the **Supporting Information**) gives an absorption length L_{abs} = 63 nm for 800 nm wavelength. The absorption is thus confined to the top surface of the chalcogenide film. We suppose that there is an extremely limited energy transport in the transverse direction, i.e.

parallel to the surface. As a result, in first-order approximation the absorption of the laser energy in the material follows the Beer-Lambert law. The fluence F as a function of film's depth z for a beam radius position r can be expressed as: $F(z, r) = F(0, r).\exp(-z / L_{abs})$, with $F(0, r) = F_0 \exp(-2.r^2 / w_0)$, where w_0 is the beam waist at the surface of the irradiated sample. Given these hypotheses, the depth at which $F(z, r) > F_{th}$ is larger at the centre of the beam spot than at its outer part. Furthermore, the fact that for different values of nominal laser fluence F_0, for a given value of F(0,r) the spatial frequencies plotted in **Figure 2-D** are quite similar tends to validate our hypothesis.

From a theoretical modelling point of view, the wrinkles formation is the result of the compressive residual internal stress of the 10 nm-thick SiN layer and the difference in thermomechanical properties between the SiN and the melted chalcogenide layer. A mechanical description of such a phenomenon by simplifying the problem to an elastic film over a viscous layer[23] also predicts that the wrinkles are the result of the compressive stress relaxation of the SiN layer. Therefore, the wavenumber of the fastest growing relaxation mode that defines the wrinkles' periodicity can be modelled by a function that depends, *inter alia* parameters, on the ratio *h/H* with *h* and *H* being respectively the thicknesses of the SiN film and that of the melted layer. More details on origin and modelling of the wrinkles formation are provided in the **Supporting Information**. This also demonstrates the tunability of the wrinkles' spatial frequency by changing the laser fluence F_0 impinging on the sample.

Finally, we tested the use of such wrinkle patterns as anti-counterfeiting tags, namely, PUF-tags. In Reference 1, it was underlined that even though wrinkle-like patterns exhibit the highest encoding capacity for such application, their use is "hampered by uses of sensitive recognition technology". This conclusion is true if the analysis is based on the ridge patterns identification, however we are going to demonstrate hereafter that by only using

publicly available routines, a high recognition ratio can be achieved. Two series of 100 PUF-tags consisting of distinct wrinkle's patterns following the above-described laser method were produced and imaged by optical microscopy. In order to test the accuracy of the recognition procedure, some patterns were measured several times in various conditions.

The first set of 100 wrinkle patterns was produced by laser irradiation of a 500 nm thick $Ge_{30}Se_{70}$ (GS) chalcogenide glass layer layer capped with a 10 nm SiN layer deposited on a Si substrate since the patterns obtained for this chalcogenide glass are really shallow, hence this is the most challenging conditions for wrinkle's patterns recognition. The second set of patterns were obtained using a GST layer, for which the fringes contrast of wrinkles is better. We note that such an improvement in that case is the result of a better contrast imaging in the optical microscopy images due to the higher refractive index of GST compound in the visible range compared to the other materials (see the optical constants of Figure S3 of the Supporting Information). We expect that the difference in optical absorption at laser wavelength will lead to different melted layers' thicknesses (see the Supporting Information also) hence impacting the fringes contrast by changing both amplitude and spatial frequency of wrinkles.

In the following, the PUF-tags are the wrinkle structures while the PUF-key is the reference image measured with an optical microscope **(Figure 3-A, B and C)**. Reading the PUF-tags can also be achieved by a conventional machine vision device. In order to simulate a real application, we have tested the influence of shift, rotation and scaling on recognition reliability. The idea behind these tests is to qualify the versatility of the PUF-tag pattern recognition method using our laser-induced wrinkle structures. Indeed, for real applications, the PUF-tag should be read without prior knowledge of how and with which device the PUF-key was measured.

A first recognition algorithm, based on the well-known Fourier Mellin transform[24] combined with skeletonization of the data has been designed. The PUF-read were simulated by randomly shifting, rotating by an angle Θ in the [0, π] range and scaled up by a scaling factor SC in range [1, 6]. The first step is then to recenter, de-rotate and re-scale the PUF-read. This is performed using a simple Fourier Mellin transform algorithm (see **Methods**). The recognition of the PUF-key is based on the structural similarity index (SSIM)[25] which provides an index ranging from 0 to 1. In **Figure 3-D** are compared the SSIM of the same randomly chosen PUF-key GS sample set (left) and GST sample set (right) to a PUF-read as a function of SC and Θ values. These results clearly show that recognition is not hampered by the orientation of the PUF-read as SSIM values higher than 0.8 are obtained for all Θ values. By opposite the scaling factor SC has a larger impact on the recognition rate since the SSIM value decreases markedly when increasing the SC's value from 1 to 6. Nevertheless, this effect can be attenuated by enlarging the area of the PUF-key and the value of SC for which the SSIM is higher than 0.7 is extended up to SC=3,6 for the GS sample set and SC=4 for GST one. Finally, by combining the two sample sets, we calculated the cross-correlation map as represented in **Figure 3-D-E**. Each PUF-read pattern, after being randomly shifted, rotated and scaled (SC values between 1 and 2), is compared to all others. The cross-correlation map shows a nearly perfect diagonal feature that reflects the accuracy of the Fourier Mellin recognition procedure. To further test this accuracy three patterns were measured under different observation conditions. This corresponds to the three islets appearing along the diagonal and eye-guided by rectangles on the **Figure 3-D**. Fourier Mellin transform, combined with skeletonization of the PUF, is a reliable method to assign a PUF-read pattern to its reference, nevertheless, such a procedure could be relatively slow. In order to speed up the process, we have developed a categorical analysis based on a convolutional neural

network (CNN). As a proof of principle, we only used the set of patterns obtained with GST. Learning basis is composed of around 2000 images of each pattern randomly shifted, scaled and rotated. Four network architectures were tested, three of them are composed of a commonly used topless network (Inception, Xception, VGG19) completed with two dense layers (1024 and 512 neurons) separated with a batch normalization layer **(Figure 4-C)**, and the last is a homemade sequential CNN **(Figure 4-E)**. Each network is trained on 24 epochs with 5000 iterations and a batch size equal to 32 (16 for Xception network). Training results are presented in **Table 1**.

Neural Network Architecture	Final accuracy
Inception	0.9980
Xception	0.9961
VGG19	0.9977
Homemade CNN	0.9968

Table 1. Accuracy index at the end of the training for the different network architectures

Best accuracy is obtained with the modified Inception model. In order to test the versatility of this network, we applied the recognizing procedure to a new set of 632 PUF-read patterns **(Figure 4-A)** composed of numerically shifted, rotated and scaled replicas of PUK-keys **(Figure 4-B)** and a pair of PUF-keys, associated to the last two classes, taken in various observation conditions. Accuracy for this particular set, whose results are presented in **Figure 4**, is equal to 94.3%. Even if some overfitting could not be completely excluded, the difference between the learning and testing rate is mainly due to the large proportion of bad quality PUF-reads in the testing set for which skeletonization procedure fails. These non-recognized patterns can be divided into two groups. The first group is composed of numerically modified PUF-read where the skeletonization generates artificial peripheral structures, which dominate the central patterns. In this case, the lack of attribution by the CNN is directly linked to numerical problems during image preparation (rotation, scaling and shift) and skeletonization. Such effects do not exist when dealing with real PUF-read. The

second group contains PUF-read acquired with a 50X-microscope objective (low resolution) while corresponding PUF-keys were recorded with a 100X-microscope objective. Fringes are then insufficiently resolved to allow correct PUF-read skeletonization. As far as PUF-read are acquired with sufficient resolution, CNN is able to fastly attribute PUF-read to PUK-key (2 minutes to analyse a 634 PUF-read set) with a high level of confidence. In order to secure the attribution process, the two methods can be combined, CNN giving the first guess in a reasonable time further checked by Fourier-Mellin transformation.

Finally, for the purpose of applications, one should discuss the stability of such wrinkles' structure against aging. Indeed, these patterns should be stable enough to be recognized for a long time. In our case, the chalcogenide film's melting temperature range is perfectly adapted for that the capping SiN layer stays in the solid state and is mechanically stable, allowing the formation of the wrinkles structures upon local chalcogenide surface melting after pulsed laser irradiation. Therefore, the main failure mechanism would be a possible recrystallization of the chalcogenide film upon ageing of extrinsic external stress. This information data retention mainly depends on the crystallization temperature of the chalcogenide film. For instance, GST is a well-known chalcogenide phase-change material that can easily crystallize. GST films exhibit a crystallization temperature of about 443 K as commonly observed for *in situ* capped and hence non-oxidized film.[26] Therefore, in that case the limit of stability against undesired recrystallization, and possible loss of wrinkles motifs, was evaluated as high as 360 K for ten years.[27]

To conclude, we demonstrated a straightforward and versatile method to generate random patterns using laser/matter interaction. We showed that the periodicity of the patterns produced in the SiN-capped chalcogenide films, hence the security level, can be

tuned by means of the impinging laser fluence. These thin film materials, which are widely used in the microelectronic industry for non-volatile resistive memories and CMOS applications, are low cost and can be easily integrated at large scale on many devices or supports. Using such an approach, either small μm^2 area can be tagged thanks to focusing of the laser beam or larger surface by using latest lasing scanning devices coupled with high average power and high repetition rate. A uniform spatial frequency and amplitude of the wrinkle patterns can also be achieved in the future by using a flat laser beam profile over the irradiated area. Finally, the recognition of the as-produced wrinkle pattern can be achieved by a simple algorithm based on publicly available routine. The overall process from the generation of the patterns to recognition is then extremely straightforward and cheap to implement on a large scale.

Experimental Section

Thin film samples preparation: All thin films were deposited in LETI's 200 mm clean room using industrial magnetron sputtering cluster tools. The thickness of the chalcogenide layers (GeTe, $Ge_{30}Se_{70}$ and $Ge_2Sb_2Te_5$) deposited on Si(100) substrate was 500 nm. In principle, a thinner chalcogenide layer can be used to generate the wrinkles as long as its thickness is larger than that of the melted layer, the latter depending mainly on the laser absorption depth at the excitation wavelength. After deposition, all films were capped *in situ* by sputtering deposition of a 10 nm-thick SiN layer in order to both prevent chalcogenide films' surface oxidation and enable later the formation of wrinkle patterns. The film thicknesses and compositions were controlled by spectroscopic ellipsometry and wavelength dispersive x-ray fluorescence (WDXRF), respectively.

Spectroscopic ellipsometry measurements: Spectroscopic ellipsometry measurements were performed in the 200-1700 nm range. Data were collected at three incidence angles (55, 65 and 75°). Analysis of the raw data was performed using WVASE 32® software. A 10 nm SiN layer deposited on a Si substrate was also measured separately in order to take into account any possible influence of the capping layer when modelling chalcogenide films' data. For chalcogenide thin film samples, the optical constants (refractive index n and extinction coefficient k) were obtained by means of modelling of the spectroscopic ellipsometry data with a Cody-Lorentz model plus one Gaussian oscillator to better account of the Urbach absorption range if needed.

Surface wrinkle patterns formation by laser beam irradiation: Two types of lasers were used. The laser AURORE is a Ti:Sapphire amplified laser system delivering pulse of 30 fs at central wavelength of 800 nm and a bandwidth of 50 nm (FWHM), 7 mJ per pulse at a 1 kHz repetition rate. The very central part of the beam is selected owing to a circular iris. The

beam is focused on the target with a f = 200mm lens down to a FWHM of 60 µm. The focused spot is imaged via a microscope objective prior to the experiment in order to measure accurately its radius (see **Figure 1-A**). The sample is mounted on a rotating holder, which allows using the full repetition rate of the laser while irradiating a pristine area each time.

Wrinkle patterns imaging and analysis: Optical microscopy measurements were performed with an Olympus BX 51 with a MPLFLN 100X/0.90 objective. Enhanced contrast can be obtained by using differential interference contrast microscopy as illustrated in the **Supporting Information Figure S1**. The Atomic Force Microscopy (AFM) images were performed at the PLACAMAT Institute in Bordeaux with a VEECO DI3100 and a Si, OMCL-AC160TS tip. The tapping mode was used for the measurement.

STEM-HAADF imaging: For electron microscopy imaging, a FIB foil of the wrinkle pattern sample was prepared in a FEI DualBeam Strata 400 by Ga+ milling using an operating voltage of 16 kV. The specimen was then finished using a lower operating voltage to reduce the surface damage on both free sides of the foil. To protect the surface of the specimen, an electron beam assisted W layer was deposited on top of the SiN layer. Then, the STEM measurements were performed on a FEI double-corrected Titan Ultimate operated at an accelerating voltage of 200 kV with an incident beam current of around 100 pA. STEM-HAADF images were recorded on an HAADF detector Fischione 3000 with a camera length of 91 mm. STEM Nano-Beam electron diffraction (NBED) patterns were recorded on a Gatan OneView camera with a camera length of 460 mm, an incident beam convergence angle of ~ 2.6 mrad and an exposure time of 100 ms per pixel. STEM EELS maps were acquired in dual-EELS mode from 200 to 2100 eV with a dispersion of 0.5 eV/channel. A standard processing

of spectra was performed in Gatan Microscopy Suite® (GMS) software to derive the elemental maps.

Pattern recognition method: All algorithms were developed using python 3.7. Fourier Mellin recognition process is composed of several steps. First, the raw image is skeletonized using the skeletonize_3d function from the skimage.morphology python package. Angle and scale are then extracted and corrected using the register_translation function (from the skimage.feature python package) applied on the respective reference and image magnitudes in log polar representation (function logPolar from OpenCV python package). The register_translation function is applied once more on the rotation/scaling corrected magnitude to get the translation between the image and the reference. Finally, translation corrected image is compared to reference using Structural SIMilarity (SSIM) (compare_ssim function from skimage.measure. This measure gives the degree of similarity (number between 0 and 1) between two pictures, focusing more on the structure than on pixel-to-pixel comparison. Convolutional Neural Network (CNN) implementation is done using Keras[28] with Tensorflow backend[29] on 2 GPU Nvidia Quadro M5000. A set of training PUF-read is first generated: 1) Entropy function from skimage.filters.rank package is used to get the center of the structure; 2) Image is then centered and cropped to fit the desired shape (299×299×3); 3) Random rotation, scaling and translation is applied on the image; 4) Noise is reduced using fastNlMeansDenoising function from OpenCV package; 5) Image is finally skeletonized. Some random Gaussian noise is added to the training image in order to limit overfitting. Training set is composed of 2030 images in each of the 112 classes used for this proof-of-principle study. Four different network architectures are tested (Inception,[30] Xception,[31] VGG19[32] and homemade CNN).

Acknowledgements

I.P. and J.G are grateful to the ANR (CASTORS project ANR-13-JS04-0002). We acknowledge the support of PLACAMAT for the AFM measurements. We thank Audrey JANNAUD from CEA-LETI for the high quality STEM foil fabrication by FIB.

Received: ((will be filled in by the editorial staff))
Revised: ((will be filled in by the editorial staff))
Published online: ((will be filled in by the editorial staff))

[1] J. Reif, in *Adv. Appl. Lasers Mater. Sci.* (Ed.: P.M. Ossi), Springer International Publishing, Cham, **2018**, pp. 63–88.
[2] J. E. E. Baglin, *Appl. Phys. Rev.* **2020**, *7*, 011601.
[3] Y. Chen, *Microelectron. Eng.* **2015**, *135*, 57.
[4] R. Arppe, T. J. Sørensen, *Nat. Rev. Chem.* **2017**, *1*, 1.
[5] Y. Gao, S. F. Al-Sarawi, D. Abbott, *Nat. Electron.* **2020**, *3*, 81.
[6] H. J. Bae, S. Bae, C. Park, S. Han, J. Kim, L. N. Kim, K. Kim, S.-H. Song, W. Park, S. Kwon, *Adv. Mater.* **2015**, *27*, 2083.
[7] N. Bowden, S. Brittain, A. G. Evans, J. W. Hutchinson, G. M. Whitesides, *Nature* **1998**, *393*, 146.
[8] Y. F. Lu, W. K. Choi, Y. Aoyagi, A. Kinomura, K. Fujii, *J. Appl. Phys.* **1996**, *80*, 7052.
[9] G. K. Giust, T. W. Sigmon, *Appl. Phys. Lett.* **1997**, *70*, 3552.
[10] J. R. Serrano, D. G. Cahill, *J. Appl. Phys.* **2002**, *92*, 7606.
[11] E. Cerda, L. Mahadevan, *Phys. Rev. Lett.* **2003**, *90*, 074302.
[12] W.-B. Jung, K. M. Cho, W.-K. Lee, T. W. Odom, H.-T. Jung, *ACS Appl. Mater. Interfaces* **2018**, *10*, 1347.
[13] D. Lencer, M. Salinga, M. Wuttig, *Adv. Mater.* **2011**, *23*, 2030.
[14] P. Noé, C. Vallée, F. Hippert, F. Fillot, J.-Y. Raty, *Semicond. Sci. Technol.* **2018**, *33*, 013002.
[15] P. Noé, A. Verdy, F. d'Acapito, J.-B. Dory, M. Bernard, G. Navarro, J.-B. Jager, J. Gaudin, J.-Y. Raty, *Sci. Adv.* **2020**, *6*, eaay2830.
[16] M. Wuttig, H. Bhaskaran, T. Taubner, *Nat. Photonics* **2017**, *11*, 465.
[17] C. Ríos, M. Stegmaier, P. Hosseini, D. Wang, T. Scherer, C. D. Wright, H. Bhaskaran, W. H. P. Pernice, *Nat. Photonics* **2015**, *9*, 725.
[18] V. Latyshev, O. Shylenko, V. Bilanych, V. Stamenkovic, V. Rizak, A. Feher, A. Kovalcikova, V. Komanicky, *ChemElectroChem* **2019**, *6*, 3264.
[19] X. Sun, A. Lotnyk, M. Ehrhardt, J. W. Gerlach, B. Rauschenbach, *Adv. Opt. Mater.* **2017**, *5*, 1700169.

[20] Q. Wang, E. T. F. Rogers, B. Gholipour, C.-M. Wang, G. Yuan, J. Teng, N. I. Zheludev, *Nat. Photonics* **2016**, *10*, 60.
[21] L. Wang, M. Eliceiri, Y. Deng, Y. Rho, W. Shou, H. Pan, J. Yao, C. P. Grigoropoulos, *Adv. Funct. Mater.* **2020**, *30*, 1910784.
[22] J. Akola, J. Larrucea, R. O. Jones, *Phys. Rev. B* **2011**, *83*, 094113.
[23] R. Huang, Z. Suo, *Int. J. Solids Struct.* **2002**, *39*, 1791.
[24] B. S. Reddy, B. N. Chatterji, *IEEE Trans. Image Process.* **1996**, *5*, 1266.
[25] Z. Wang, A. C. Bovik, H. R. Sheikh, E. P. Simoncelli, *IEEE Trans. Image Process.* **2004**, *13*, 600.
[26] P. Noé, C. Sabbione, N. Bernier, N. Castellani, F. Fillot, F. Hippert, *Acta Mater.* **2016**, *110*, 142.
[27] P. Noé, F. Hippert, in *Phase Change Mem. Device Phys. Reliab. Appl.* (Ed.: A. Redaelli), Springer International Publishing, Cham, **2018**, pp. 125–179.
[28] F. Chollet, "Deep Learning for humans," can be found under https://github.com/keras-team/keras, **2015**.
[29] M. Abadi, A. Agarwal, P. Barham, E. Brevdo, Z. Chen, C. Citro, G. S. Corrado, A. Davis, J. Dean, M. Devin, S. Ghemawat, I. Goodfellow, A. Harp, G. Irving, M. Isard, Y. Jia, R. Jozefowicz, L. Kaiser, M. Kudlur, J. Levenberg, D. Mane, R. Monga, S. Moore, D. Murray, C. Olah, M. Schuster, J. Shlens, B. Steiner, I. Sutskever, K. Talwar, P. Tucker, V. Vanhoucke, V. Vasudevan, F. Viegas, O. Vinyals, P. Warden, M. Wattenberg, M. Wicke, Y. Yu, X. Zheng, **n.d.**, 19.
[30] C. Szegedy, S. Ioffe, V. Vanhoucke, A. Alemi, *ArXiv160207261 Cs* **2016**.
[31] F. Chollet, *ArXiv161002357 Cs* **2017**.
[32] K. Simonyan, A. Zisserman, *ArXiv14091556 Cs* **2015**.

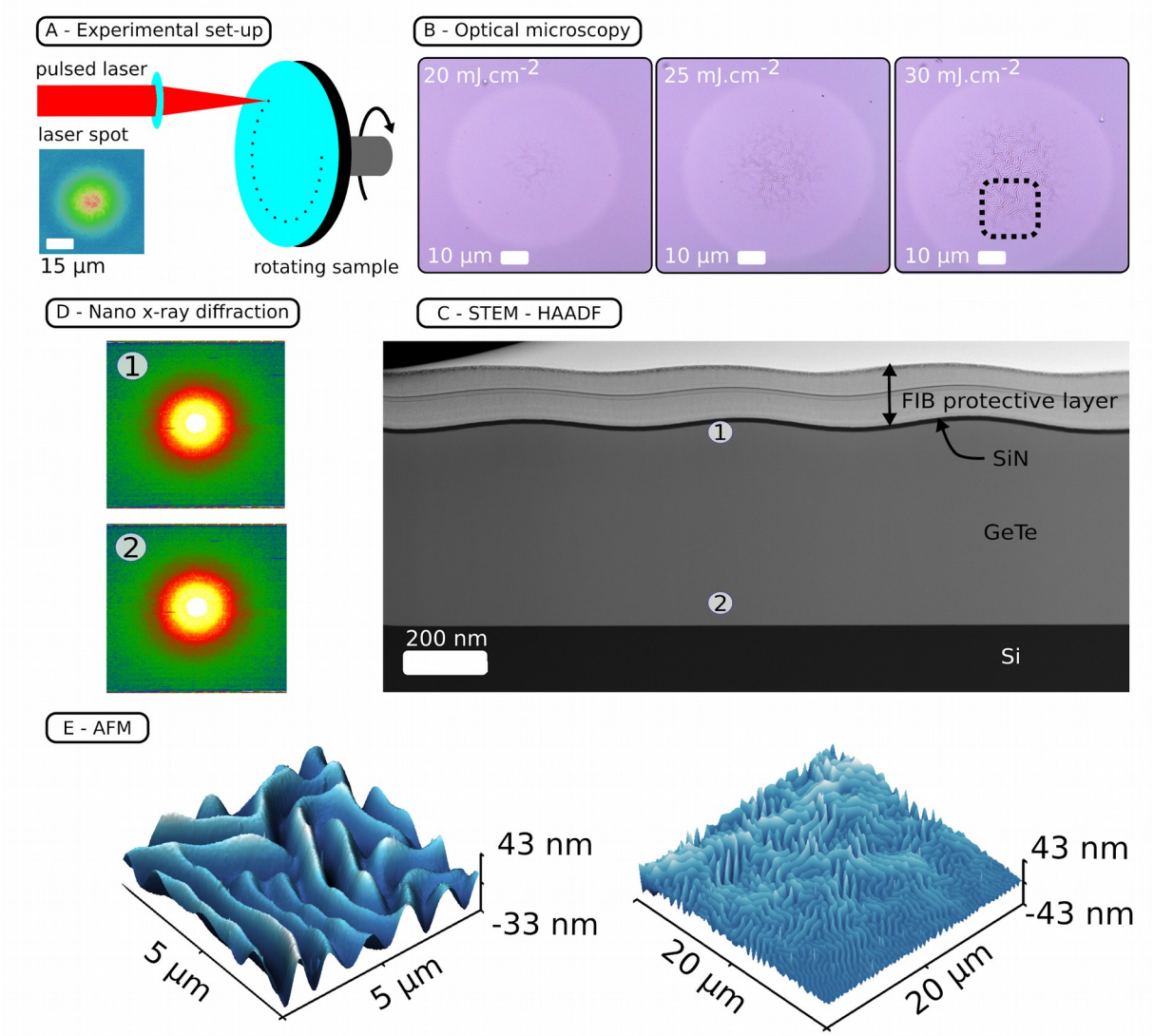

Figure 1. Optical experimental setup and analysis of the obtained patterns after pulsed laser irradiation of a 500 nm-thick GeTe thin film capped with a 10 nm SiN layer and deposited on a Si bulk substrate.

A) Simplified scheme of the experimental set-up showing the 1kHz pulsed laser beam focused by a lens on the thin film sample surface mounted on a rotating sample holder.
B) Microscope images of the surface of irradiated samples for three different laser fluence of F_0 = 20, 25 and 30 mJ.cm^{-2}.
C) Cross sectional STEM – HAADF image of the SiN-capped 500nm thick GeTe thin film sample acquired at the central part of the irradiated area with a laser fluence F_0 = 30 mJ.cm^{-2}. The 10 nm-thick SiN capping layer appears in black and is covered by a protective layer used for the STEM foil preparation by FIB. No change of the microstructure of the GeTe film is observable over the whole film thickness. The materials is still amorphous after laser exposure as evidenced by the two electron beam diffraction patterns of Figure (D) acquired at positions 1 and 2 marked on the STEM image
D) Nanobeam electron diffraction (NBED) patterns acquired at positions 1 (under the surface, corresponding to the melted volume) and 2 (close to the Si substrate in a film's zone non affected by the laser) as indicated on the STEM-HAADF image in C. Only diffuse scattering rings corresponding to a disordered amorphous structure are visible without any presence of a diffraction pattern due to any crystallites.
E) AFM images acquired in the irradiated part of the film with laser fluence F_0 = 30 mJ.cm^{-2}. The 20x20 µm² image was acquired in the dashed square plotted in Figure 1-B and the 5x5 µm² image corresponds to the very centre of the irradiated pattern.

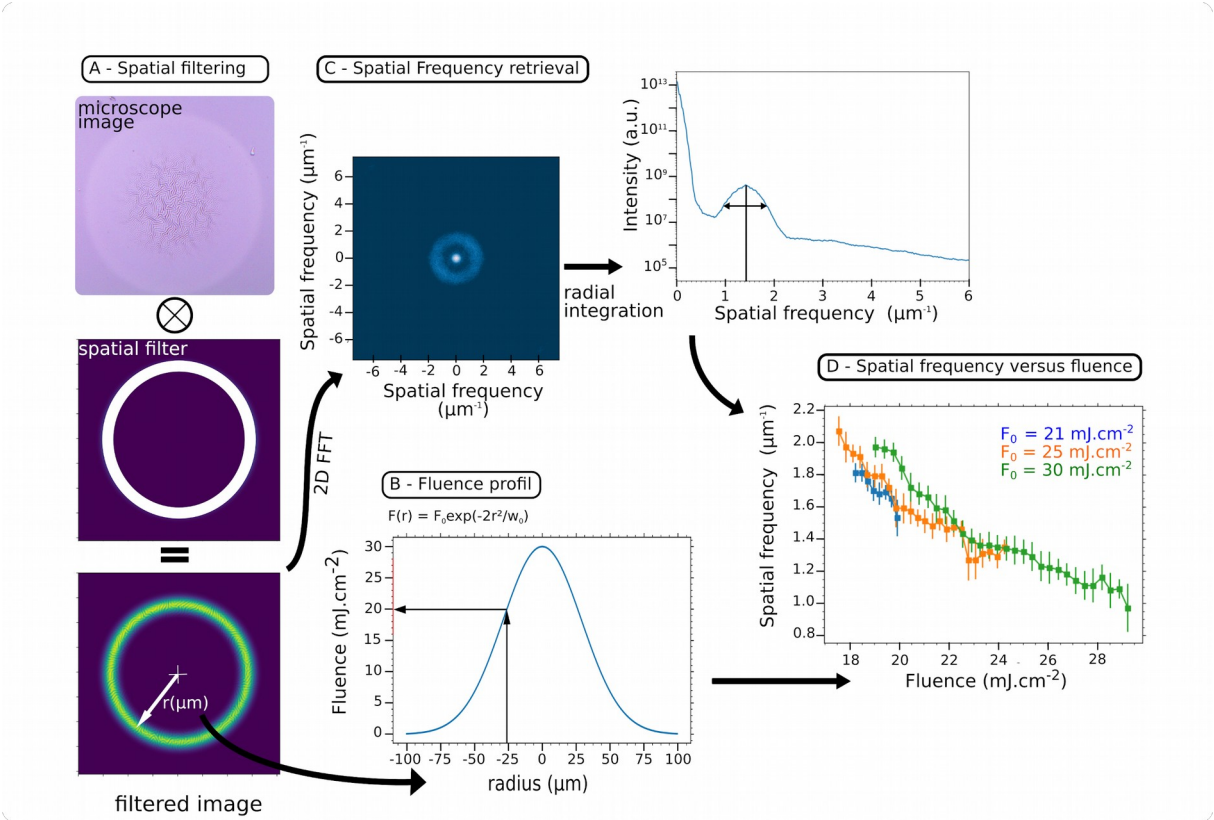

Figure 2. Analysis of the wrinkles' spatial frequency as a function of the impinging fluence determined by selecting different rings of various radius in the wrinkles' circular area.

A) The optical microscopy images are spatially filtered in order to select a ring at a given radius corresponding to a constant fluence value.

B) Knowing the radius, one can determine the fluence F(r) at each radius value r, as the beam profile is Gaussian.

C) The wrinkles' spatial frequency is determined by the position of the peak visible on radial integration of 2D-FFT of the filtered image.

D) Plot of the spatial frequency vs the laser fluence. For all three nominal fluences F_0 tested, the spatial frequency of the wrinkles progressively decreases as the fluence increases. The error bars reported on the data points correspond to the full width at half-maximum (FWHM) of the spatial frequency peaks.

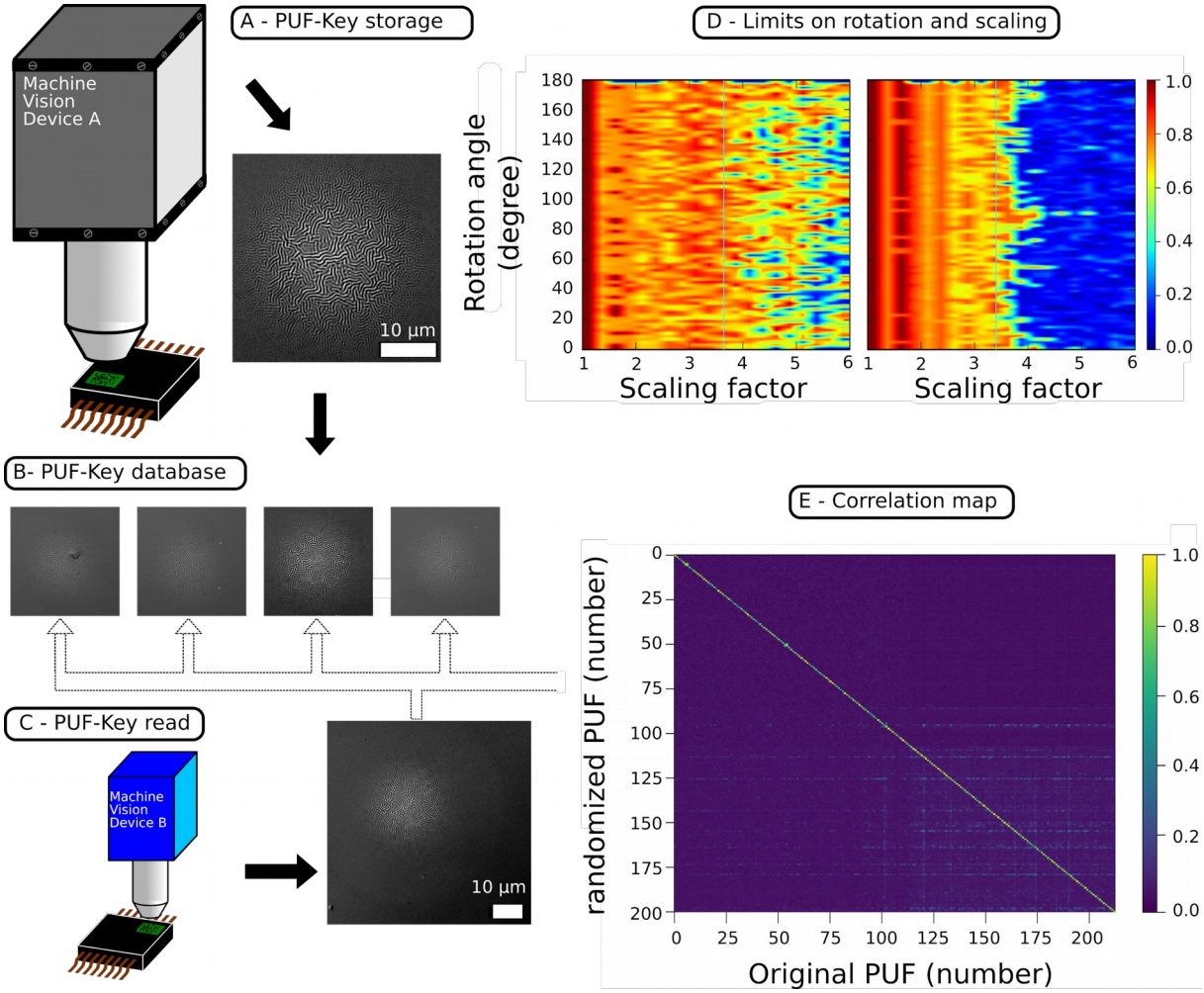

Figure 3. PUF based anti-counterfeiting process:

A) Registration of the PUF-key during the manufacturing process.

B) The PUF-key is added to the database.

C) The PUF-Key is then read by the end user and identified using a dedicated software.

D) Influence of the rotation and scaling on the recognition based on the SSIM index. SSIM index plotted as a function of scaling factor and rotation angle for GST (left) and GS (right) sample sets.

E) Correlation map, i.e. value of the SSIM, in GST and GS.

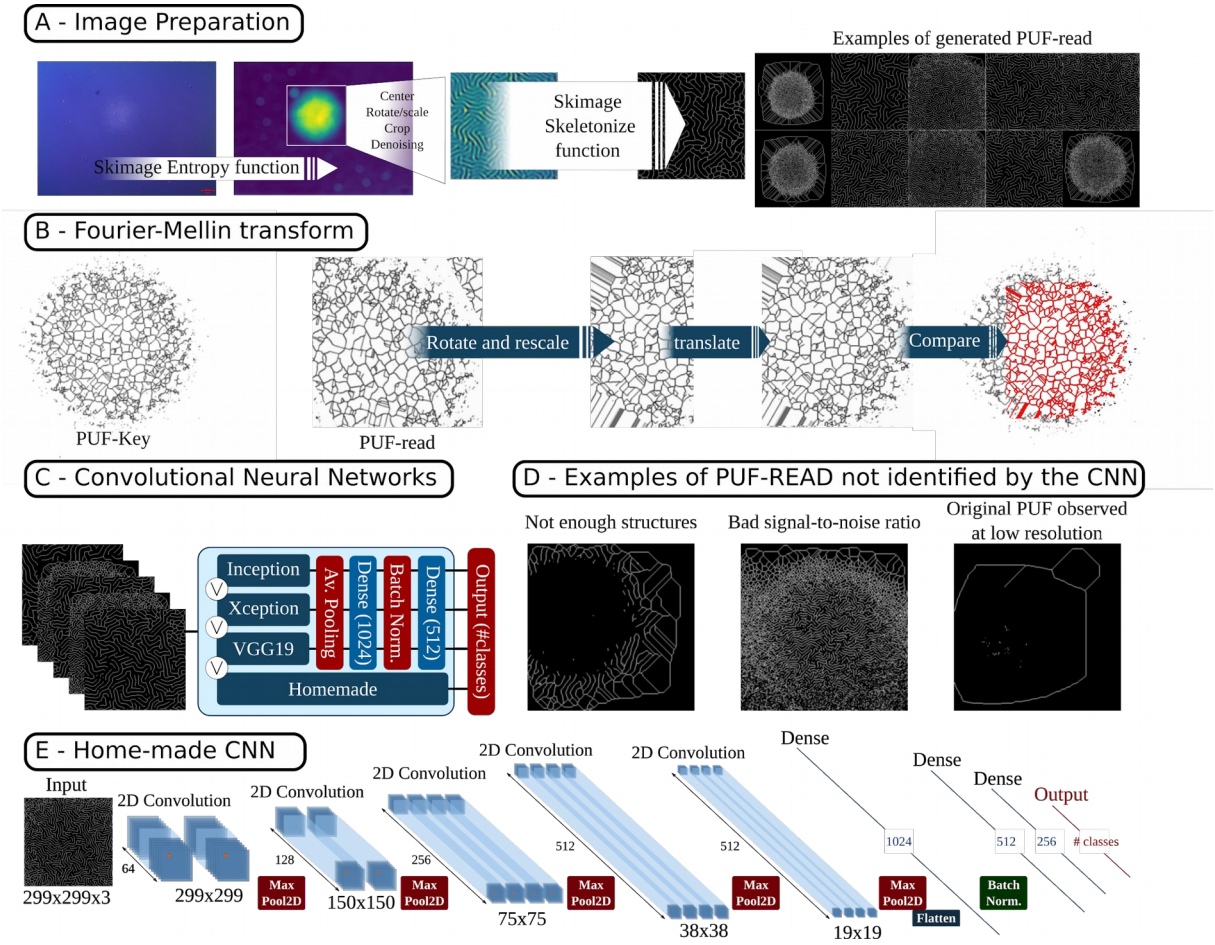

Figure 4. Schematic of the PUF-read recognition processes.

A) Description of the image preparation, from raw PUF-read picture to skeletonization.

B) Example of recognition procedure based on Fourier-Mellin transform and final comparison between PUF-key and PUF-read artificially scaled, rotated and shifted.

C) Convolutional neural network general architecture showing the four different networks used in the recognition procedure (see text).

D) Some examples of non-recognized PUF-Read where skeletonization failed.

E) Detailed description of the homemade convolutional neural network.

The formation of random patterns induced by a laser pulse focused on amorphous Ge-based chalcogenide thin film capped with a very thin SiN layer is demonstrated. These non-

deterministic surface patterns are sub-100 nm height wrinkles with a sub µm periodicity which depends on the impinging laser fluence. Application as physical unclonable functions is demonstrated using a dedicated fast recognition algorithm.

Keyword: Laser functionalization surface process

Paloma Martinez, Irene Papagiannouli, Dominique Descamps, Stéphane Petit, Joël Marthelot, Anna Lévy, Baptiste Fabre, Jean-Baptiste Dory, Nicolas Bernier, Jean-Yves Raty, Pierre Noé and Jérôme Gaudin

Laser generation of sub-micron wrinkles in a chalcogenide glass film as physical unclonable functions

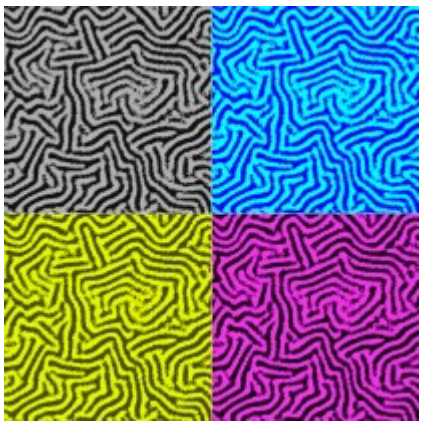

Supporting Information

Laser generation of sub-micron wrinkles in a chalcogenide glass film as physical unclonable functions

Paloma Martinez, Irene Papagiannouli, Dominique Descamps, Stéphane Petit, Joël Marthelot, Anna Lévy, Baptiste Fabre, Jean-Baptiste Dory, Nicolas Bernier, Jean-Yves Raty, Pierre Noé and Jérôme Gaudin

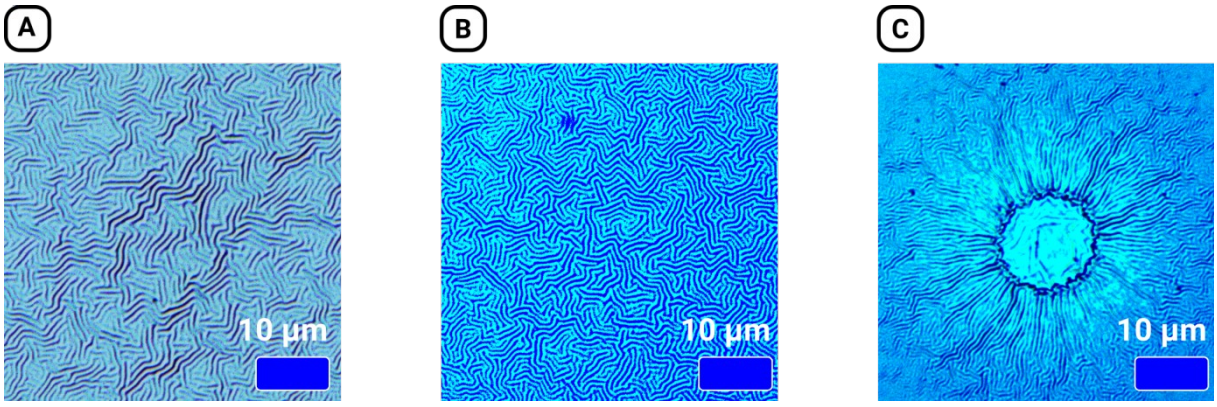

Figure S1. *Wrinkle patterns obtained on a 500 nm* $Ge_2Sb_2Te_5$ *alloy thin film irradiated by means of a 1030 nm Ytterbium laser based pulsed laser with (A) a pulse duration of 400 fs, (B) a pulse duration of 400 ps and (C) example of case where the ablation threshold was reached for a pulse duration of 400 fs with the Ti:Sapphire laser at 80 nm.* In (C), *the central part of the layers was ablated resulting in the lack of pattern and the orientation of the surrounding pattern normal to the border of the ablated area.*

The 100-kHz Ytterbium laser is based on chirped-pulse amplification in fibers and delivers 400 fs laser pulses at the central wavelength of 1030 nm with a spectral bandwidth of 6 nm at a repetition rate of 100 kHz. A downstream BBO Pockels cell pulse picker allows to decrease on-demand the repetition rate down to the single shot operation on target without changing the spatial, spectral and temporal properties of the laser beam. With more than 100 µJ pulse energy at the output of the laser, the final energy on target is controlled by the combination of a half-waveplate and a thin-film polarizer. Finally, pulse duration can be varied from 400 fs to 400 ps by a downstream grating-based dispersion delay line.

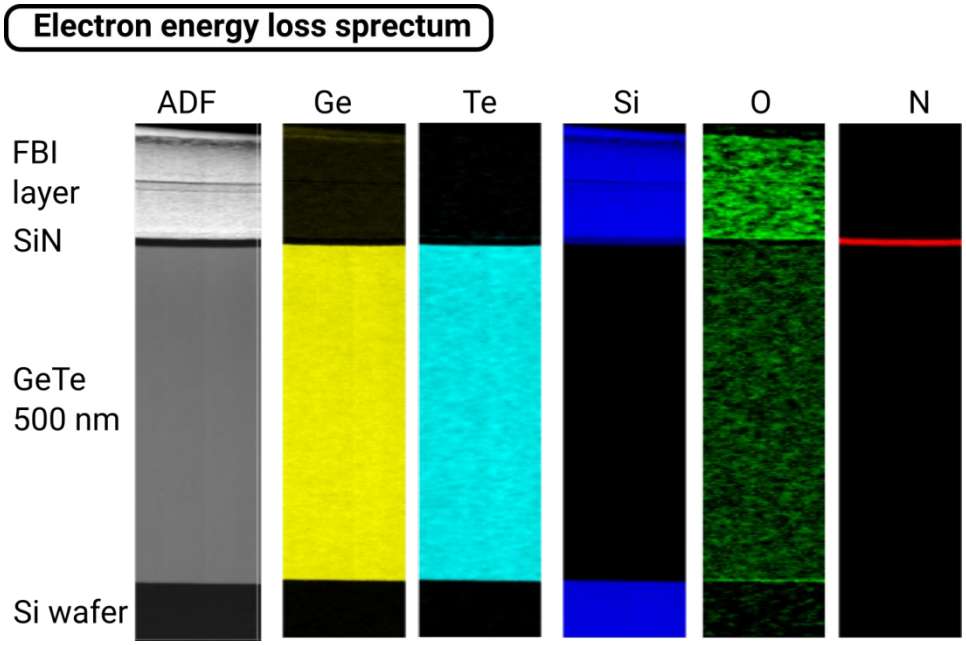

Figure S2. *Cross-sectional element maps for Ge, Te, Si, O and N atoms on the GeTe thin film sample after laser irradiation obtained by means of Electron Energy Loss Spectroscopy (EELS) measurements. The annular Dark Field (ADF) image shows the different stacked layers from top to bottom: the FIB protective layer deposited for the STEM foil preparation by FIB, the 10-nm thick SiN capping layer (black), the 500 nm GeTe layer (grey) and the Si substrate (black). No element segregation is visible over the whole film thickness.*

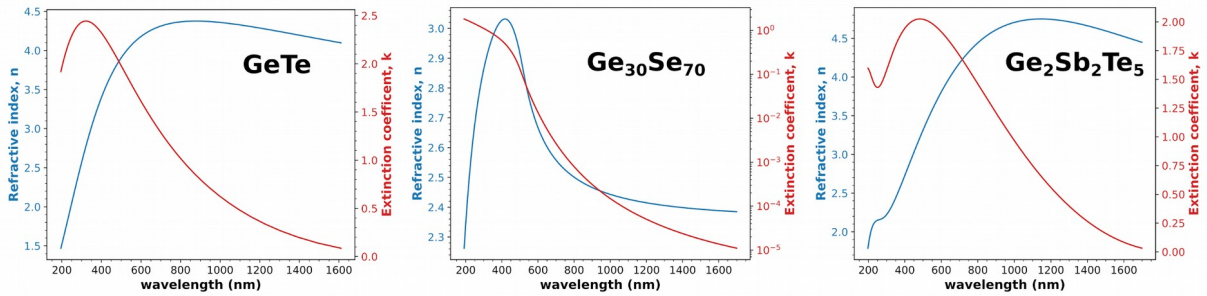

Figure S3. *Optical constants of the pristine as deposited amorphous GeTe, $Ge_{30}Se_{70}$ and $Ge_2Sb_2Te_5$ layer deduced from modelling of spectroscopic ellipsometry measurements.*

Origin and modelling of the physical process behind the surface wrinkles' formation:

The 10 nm-thick SiN layer deposited by means of magnetron sputtering technique exhibits a residual internal stress due to thermal coefficient expansion mismatch between the SiN and its underlying substrate made of the chalcogenide layer over the Si bulk substrate.

The laser pulse leads to the surface melting of the chalcogenide layer followed by solidification of the melted layer. The thickness of the melted layer H in the chalcogenide layer depends on the laser fluence F_0. The bilayer system can be approximated as a compressed SiN thin

film of thickness h, Young modulus E, Poisson ratio ν and residual biaxial strain ε_0 deposited on a viscous layer of thickness H. Wrinkles form in the SiN film to reduce the elastic energy. The stability of the compressed elastic film on a viscous layer of uniform thickness can be studied by linear perturbation analysis [1] to predict the critical wave number and the growth rate of the unstable modes. The wavenumber of the fastest unstable mode, which is a function of the compressive strain, increases with the thickness ratio between the elastic film and the viscous layer and does not depend on the viscosity of the viscous layer. We observed that the spatial frequency of the wrinkles decreases when increasing the laser fluence (see Figure 2-D of the main text). Indeed, the thickness of the melted layer increases with the laser fluence, hence decreasing the thickness ratio h/H and thus resulting in a decrease of the spatial frequency of the wrinkles.

To get more quantitative, we measured the residual internal compressive stress of the SiN thin film deposited on a Si substrate by means of wafer curvature measurement and by applying the simple Stoney's formula.[2] The wafer curvature change before and after deposition of the SiN layer is related to the residual stress σ_0 of the latter through Stoney's law. We found a residual compressive stress value σ_0= -0.92 GPa for our 10 nm SiN thin film for which we assumed a Poisson ratio ν = 0.27 and a Young modulus E = 210 GPa.[3] Such a stress value corresponds to a residual strain ε_0 = σ_0 /E = -0.44 %. Following the model in reference[1], the fastest growing spatial wavenumber is close to $\frac{\sqrt{\square}}{\square}$ in the limit of a small thickness ratio ($h/H \rightarrow \infty$) and tends to $\frac{\sqrt{\square}}{\square}$ in the limit of an infinitely thick viscous layer ($h/H \rightarrow 0$).

Finally, the prediction of the fastest growing wavenumber by using the estimated residual compressive strain of the SiN layer leads to a calculated wrinkles' spatial frequency varying from 2.4 to 3.3 μm^{-1} (within infinitely thick to small thickness ratios limits). Even if these values are slightly over estimated, they are however consistent with the spatial frequencies observed experimentally in Figure 2-D of the main text. The difference between analytical model and experimental observations has probably two main origins. The first source of error is related to the values used for the mechanical properties of the SiN film that certainly differ from the experimental ones. Secondly, the predictions of the fastest growing wavenumber are formally derived in the simpler case of a thin film deposited over a viscous layer of constant thickness. However, in our experiment the thickness of melted chalcogenide layer is varying along the laser spot radius due to the Gaussian profile of the laser beam used to melt and form the viscous layer.

[1] R. Huang, Z. Suo, *Int. J. Solids Struct.* **2002**, *39*, 1791.

[2] B. Ben Yahia, M. S. Amara, M. Gallard, N. Burle, S. Escoubas, C. Guichet, M. Putero, C. Mocuta, M.-I. Richard, R. Chahine, C. Sabbione, M. Bernard, L. Fellouh, P. Noé, O. Thomas, *Micro Nano Eng.* **2018**, *1*, 63.

[3] M. Vila, D. Cáceres, C. Prieto, *J. Appl. Phys.* **2003**, *94*, 7868.